Nano Research

Open Access

Research Article

The effect of room temperature magnetic field on photoluminescence of Mn:$CsPbBr_3$ quantum dots prepared by one-pot method in air

Mengwei Chen[1], Chenguang Shen[1], Wei Huang[1], Yingping Yang[1], and Jie Shen[2] ✉

[1] *Department of Physics, School of Physics and Mechanics, Wuhan University of Technology, Wuhan 430070, China*
[2] *State Key Laboratory of Advanced Technology for Materials Synthesis and Processing, School of Materials Science and Engineering, Wuhan University of Technology, Wuhan 430070, China*

Cite this article: *Nano Research*, **2025**, *18*, 94907268. https://doi.org/10.26599/NR.2025.94907268

ABSTRACT: The generation and manipulation of spin-polarized electrons at room temperature are essential for the development of advanced spin-optoelectronic devices. In this work, a one-pot method was used to successfully synthesize homogenous Mn:$CsPbBr_3$ perovskite quantum dots in air with particle sizes of 7−8 nm. The effects of Mn doping on the structure, optical and magnetic properties of $CsPbBr_3$ quantum dots were investigated. The findings demonstrated proper Mn doping improved the crystallinity and photoluminescence (PL) of quantum dots. The prepared quantum dots have a narrow full width at half maximum emission (FWHM) of about 17−20 nm. The magnetic properties of the doped samples and the effect of the magnetic field on the PL spectra properties were analyzed. The results show that trace Mn doping can improve the room-temperature ferromagnetism of $CsPbBr_3$ quantum dots. Doping with magnetic elements makes $CsPbBr_3$ quantum dots more responsive to the applied magnetic field. Even at a lower 50 mT magnetic field, the PL peak of Mn:$CsPbBr_3$ still declined 5.91%. Mn:$CsPbBr_3$ quantum dots are a new type of multifunctional material that is beneficial to spintronics research. This work demonstrates a low-cost synthesis method. It should make all-inorganic perovskite quantum dots a promising material for room-temperature spin optoelectronic devices.

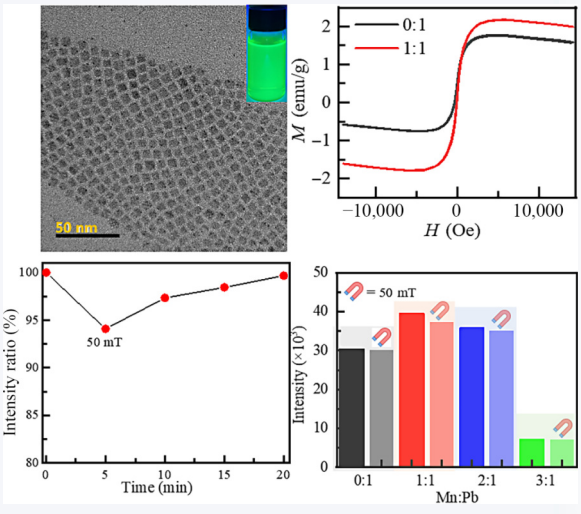

KEYWORDS: $CsPbBr_3$ quantum dots, Mn doping, one-pot method, ferromagnetism, magnetic field

1 Introduction

The rise of spintronics has increased interest in spintronic materials [1–5]. Researchers have fabricated various spintronic devices, such as spin light-emitting diodes [6–7] and spin field-effect transistors [8, 9], which are expected to serve as alternatives to traditional charge-based semiconductor devices. Therefore, the synthesis of functional materials for high-performance spintronic applications is crucial for the future development of advanced and efficient spintronic devices. Researchers have studied a large number of spintronic materials so far, including inorganic semiconductors [10], organic semiconductors (OSC) [11, 12], two-dimensional materials (2DM) [13, 14], and organic–inorganic hybrid perovskites (OIHP) [15, 16].

Metal halide perovskites (MHPs) have great optical and electronic properties, low cost, and can be made using a solution process [17–20]. They are promising for optoelectronic devices [17, 21, 22]. However, they seldom show magnetism, which imposes significant limitations on their application in the field of spintronics. Doping the magnetic element Mn can regulate the optical and magnetic properties of lead halide perovskites, improve structural stability, and reduce lead content. At the same time, doping Mn can extend the carrier lifetime and suppress charge recombination by manipulating the spin-polarized electrons, and the crystallinity of MHPs will not be excessively sacrificed. It is a promising and workable method to improve the photoelectric performance of

Received: December 3, 2024; **Revised:** January 12, 2025
Accepted: January 22, 2025

✉Address correspondence to shenjie@whut.edu.cn

MHPs and is expected to be used to manufacture high-performance optoelectronic devices. Nafradi et al. [23] reported the synthesis of ferromagnetic MAMn:PbI_3 material, showing the extension of photovoltaics to magnetism. They found that without heating the spin structure, the photoexcited electrons melted the local magnetic order quickly through the Ruderman–Kittel–Kasuya–Yosida interaction, indicating that the halide perovskite may be a feasible choice for spintronic devices. Nagalingam et al. [24] doped Mn^{2+}/Mn^{3+} ions into $MAPbI_3$ thin films, and achieved room-temperature ferromagnetism. It was due to strong double and super exchange interactions between Mn^{2+}–I^-–Mn^{3+} ions. Compared to organic–inorganic hybrid perovskite materials, all inorganic perovskite has better stability. In recent years, there has been some progress in doping Mn in $CsPbX_3$ (X = Cl, Br, I). Mohammed et al. [25] found that inorganic $CsPbBr_3$ becomes a ferromagnetic material by introducing Mn through first-principles calculations, and it exhibits a large magnetic moment of 4.995 mB, which mainly results from localized d states of the Mn atoms. In terms of all-inorganic perovskite quantum dots, Parobek et al. [26–27] used different methods to dope Mn^{2+} ions into $CsPbCl_3$ and $CsPb(Cl/Br)_3$. Subsequently, Mn-doped all-inorganic perovskite quantum dots have also been continuously studied and applied [28, 29]. But the research mainly focuses on the structure, optical properties, and applications. There is relatively little research on the magnetism of all-inorganic perovskite quantum dots. The study of integrating magnetism into $CsPbBr_3$ quantum dots through Mn doping is of great significance for their use in room temperature spin electron devices.

In view of this, Mn:$CsPbBr_3$ quantum dots were synthesized in air by a simple one-pot method. The experimental results show that uniform doping of Mn affects the optical and magnetic properties of $CsPbBr_3$. It improves the response to the magnetic field and provides a new choice for the development of spintronic devices at room temperature. The development of magnetic metal halide perovskites will create more opportunities for controlling spins in electrons in this advanced, multifunctional material.

2 Experimental

2.1 Materials and reagents

Cesium carbonate (Cs_2CO_3, 99.9%), lead bromide ($PbBr_2$, 99.9%), octadecene (ODE, > 90%), oleylamine (OAm, 80%–90%), trioctylphosphine (TOP, 90%), oleic acid (OA), and methyl acetate (MeOAc, AR, ≥ 98%) were purchased from Macklin (China). $MnBr_2$ (98%) was purchased from Sigma-Aldrich (Shanghai) Trading Co. Ltd. N-Hexane (≥ 97%) was purchased from China National Pharmaceutical Chemical Reagents Company. All materials were used without further purification.

2.2 Synthesis and purification of Mn:$CsPbBr_3$ quantum dots

Synthesis of Mn:$CsPbBr_3$ quantum dots: $CsPbBr_3$ quantum dots were synthesized by one-pot method. Firstly, 0.068 mmol Cs_2CO_3 and 0.376 mmol $PbBr_2$ were weighed and then placed in a 50 mL three-necked round bottom flask inside a nitrogen environment glove box. The mixture was dissolved in 10 mL ODE, 1 mL OAm, 1 mL TOP, and 1 mL OA in the air environment. The mixture was stirred and heated to 120 °C, maintained at 120 °C, and continued to stir for 30 min. The three-necked round bottom flask was cooled to room temperature in cold water to stop the reaction. Mn:$CsPbBr_3$ quantum dots with Mn:Pb molar ratios of 1:1, 2:1, and 3:1 were sequentially added to the mixture before the reaction with the corresponding molar ratio of $MnBr_2$.

Isolation and purification Mn:$CsPbBr_3$ quantum dots: An equal volume of methyl acetate was added to the obtained product, centrifuged at 10,000 rpm for 5 min, the quantum dots were separated from the crude solution. The supernatant was discarded. Then 10 mL of methyl acetate was added to the precipitate, centrifuged at 10,000 rpm for 5 min and the supernatant was discarded. Washing can be repeated as needed. The precipitate was dispersed in 3 mL n-hexane and centrifuged at 3000 rpm for 5 min to sort out the quantum dots, and the supernatant was taken out for use.

2.3 Characterization

Transmission electron microscopy (TEM) images, high-resolution TEM (HRTEM) images, selected area electron diffraction (SAED) images, and energy dispersive X-ray spectroscopy (EDS) of Mn:$CsPbBr_3$ quantum dots were obtained using a 200 kV field emission high-resolution TEM (JEM-2100F, JEOL, Japan). The atomic ratio of Mn to Pb in the Mn:$CsPbBr_3$ quantum dots was measured by inductively coupled plasma-optical emission spectroscopy (ICP-OES) (Teledyne Leeman Labs, Prodigy7, USA). The crystallization and crystal structure of samples were characterized by X-ray diffraction (XRD, Empyrean, Malvern Panalytical, UK) using Cu Kα radiation (λ = 1.54 Å) with a diffraction angle ranging from 5° to 80°. X-ray photoelectron spectroscopy (XPS) (AXIS SUPRA, Shimadzu, Japan) was used to analyze the elemental composition of the samples and the bonding between elements. An ultraviolet–visible spectrophotometer (UV-2600, Shimadzu, Japan) was used to measure the absorption properties of quantum dots. Steady-state photoluminescence (PL) spectra were recorded by a fluorescence spectrometer (RF-6000, Shimadzu, Japan), and the excitation wavelength was 385 nm. Time-resolved photoluminescence spectroscopy (TRPL) was measured by a modular stable transient fluorescence spectrometer (Fluorolog-QM, HORIBA, Japan) to characterize the carrier lifetime of quantum dots. Vibrating sample magnetometer (VSM) (7400S, LakeShor, USA) was used to test the hysteresis loop of the samples, and the applied magnetic field range was −15,000–15,000 Oe. The hysteresis loop was used to characterize the static magnetic properties such as saturation magnetization and coercivity of the samples.

3 Results and discussion

Mn:$CsPbBr_3$ quantum dots with different Mn^{2+} doping concentrations were synthesized by one-pot method. The molar ratios of Mn and Pb in the four samples were 0:1, 1:1, 2:1, and 3:1 (the four samples were represented by 0:1, 1:1, 2:1, and 3:1, respectively), and the phase and morphology were characterized. Figures 1(a)–1(d) are the TEM images of $CsPbBr_3$ QDs with different Mn doping concentrations. It is shown that nanoparticles with a cubic shape are formed and there is no agglomeration. The illustrations are photos of the product in n-hexane. It was illuminated by a UV lamp with a 365 nm wavelength, showing bright green fluorescence. TEM analysis shows that quantum dot size decreases with higher Mn concentration. It drops from 8.38 nm for pure $CsPbBr_3$ nanocrystals (Figs. 1(a) and 1(e)) to 7.9 nm for sample 1:1 (Figs. 1(b) and 1(f)), 7.81 nm for sample 2:1 (Figs. 1(c)

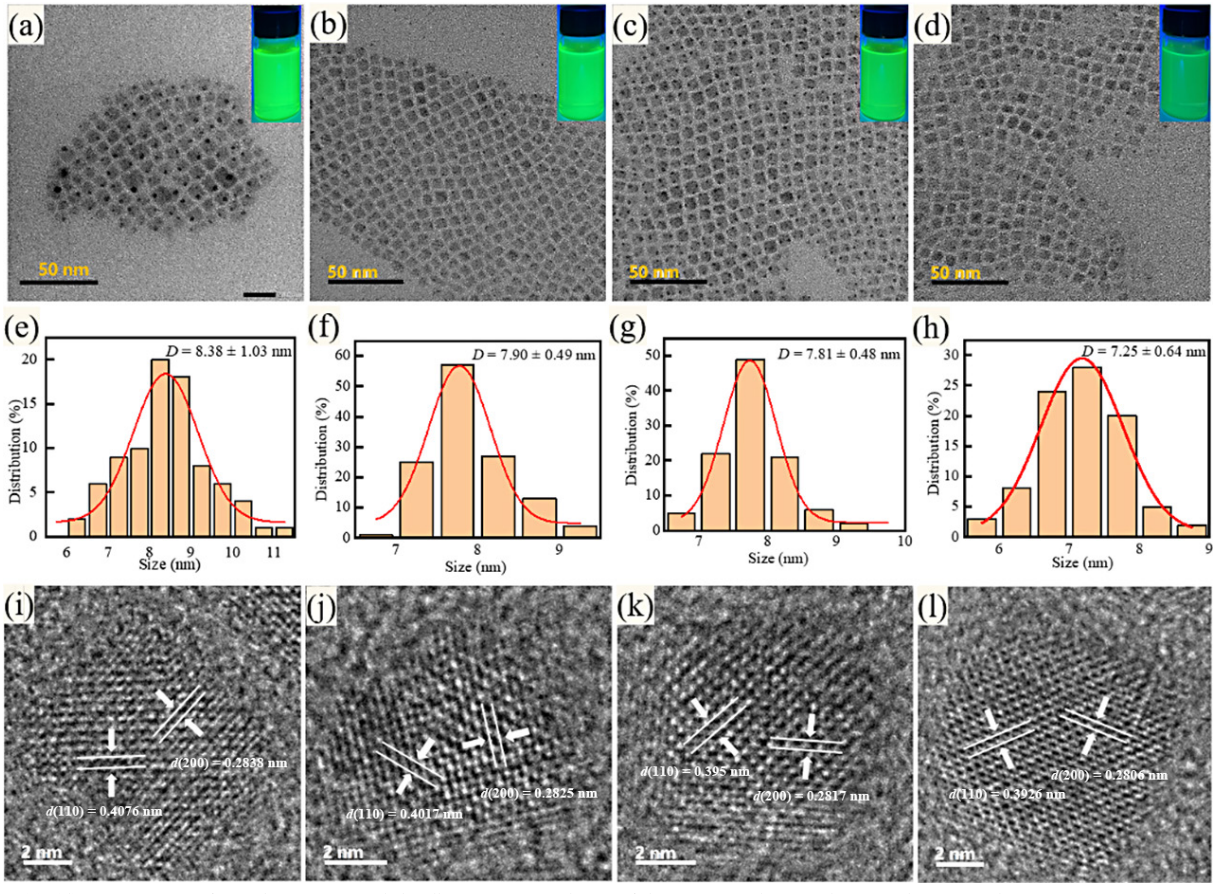

Figure 1 (a)–(d) TEM images of samples 0:1–3:1, and the illustrations are photos of the corresponding product in n-hexane under 365 nm UV excitation; (e)–(h) particle sizes distribution; (i)–(l) HRTEM images.

and 1(g)), and 7.25 nm for sample 3:1 (Figs. 1(d) and 1(h)). This is slightly larger than the exciton Bohr diameter (7 nm) [30]. The TEM images show that the size distribution of quantum dots (samples 1:1 and 2:1) are more uniform after Mn doping. The doping of Mn increases the defect formation energy and promotes a nearly uniform local structural order of perovskite quantum dots, resulting in improved size uniformity, which is beneficial for improving the optical properties of quantum dots. The uniformity of sample 3:1 began to deteriorate, possibly due to the induction of new phases by excessive doping.

The HRTEM images are shown in Figs. 1(i)–1(l). Table 1 shows the interplanar spacing of four different quantum dots and standard PDF (PDF#54-0752). The lattice constants of the (110) crystal planes of the four samples 0:1, 1:1, 2:1, and 3:1 are 4.076, 4.017, 3.95 and 3.926 Å, respectively, and the lattice constants of the (200) crystal planes are 2.838, 2.825, 2.817, and 2.806 Å, respectively. The lattice spacing of $CsPbBr_3$ is close to the standard card PDF#54-0752. The increase in Mn^{2+} doping amount decreases the spacing of the (110) and (200) crystal planes. The lattice shrinkage of Mn^{2+} doped $CsPbBr_3$ quantum dots is mainly due to the substitution of smaller Mn^{2+} ions (about 0.8 Å) for larger Pb^{2+} ions (about 1.2 Å).

Table 1 Interplanar spacing of samples 0:1 to 3:1 and standard PDF

Sample	Crystal face	Interplanar distance (Å)
PDF#54-0752	(110)	4.12
	(200)	2.915
0:1	(110)	4.076
	(200)	2.838
1:1	(110)	4.017
	(200)	2.825
2:1	(110)	3.95
	(200)	2.817
3:1	(110)	3.926
	(200)	2.806

Although a large amount of Mn^{2+} was added to the reaction precursor, not all of them were doped into the host crystal, and further qualitative and quantitative characterization of Mn in the product was needed. The structure of XRD powder diffraction patterns of four different products was analyzed by XRD. It also evaluated the effect of Mn doping on crystallization and crystal phase by measuring different Mn concentrations. Figure 2 shows the XRD patterns of Mn:$CsPbBr_3$ quantum dots with samples of 0:1, 1:1, 2:1, and 3:1. In Fig. 2, sharp and strong peaks appeared in samples 0:1, 1:1 and 2:1, indicating that the crystallization effect was good, and the crystallinity of sample 3:1 was poor, consistent with the TEM results.

The XRD spectra of $CsPbBr_3$ quantum dots match the standard $CsPbBr_3$ (PDF#54-0752) in both peak position and intensity. This confirms that the prepared $CsPbBr_3$ quantum dots have high crystallinity and form a cubic phase. The larger Pb^{2+} ions in the octahedral unit are replaced by a small amount of the smaller dopant Mn^{2+} ions. This causes lattice contraction. So, the XRD pattern of the Mn:$CsPbBr_3$ quantum dots is slightly shifted to a higher angle than that of the host $CsPbBr_3$ quantum dots, and the

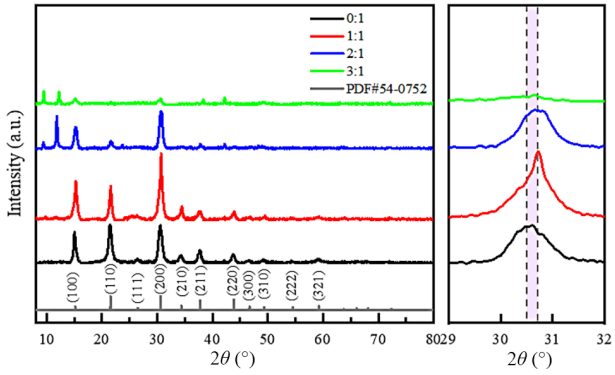

Figure 2 XRD patterns of samples 0:1–3:1 and standard PDF.

observed angular displacement of (200) peak is about 0.17° (0:1 is 30.55°, 1:1 is 30.72°). This proves that Mn^{2+} is successfully combined into the perovskite lattice. Also, the main peak of sample 1:1 is stronger than sample 0:1. Samples 2:1 and 3:1 show two new peaks at 9.41°, 11.85° and 9.47°, 12.23°, respectively, due to residual organic compounds in the samples. Under the same purification treatment, there were more residual organic compounds in samples 2:1 and 3:1. The SAED patterns of samples 0:1 and 1:1 were further tested as shown in Fig. 3. It shows the existence of cubic phase (100) and (200) planes indicating that the perovskite structure is not destroyed. The diffraction ring of sample 1:1 is clearer and the crystallinity is better, which is the same as the XRD test conclusion.

Figure 4 shows the EDS element mapping diagrams of quantum dots, which proves that the elements are distributed evenly across a large scale. The uniform distribution of Mn means that the added

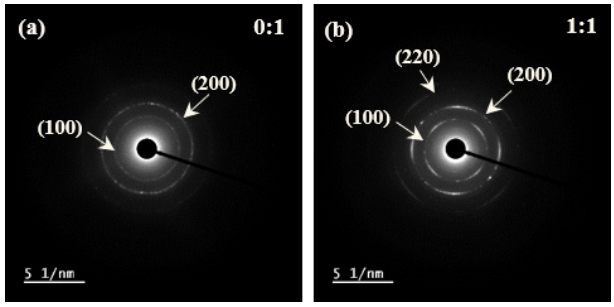

Figure 3 SAED patterns of (a) sample 0:1 and (b) sample 1:1.

Mn does not accumulate at the grain boundary. Instead, it participates in forming the lattice. Table 2 is the result of atomic ratio analysis of four samples. As the molar ratio rises, the product's Mn content increases first and then decreases. It is consistent with the movement trend of the main peak in the XRD test results. Mn accounted for 2.61% of the total content of Mn and Pb in sample 1:1.

The actual compositions of sample 0:1 and 1:1 were analyzed by XPS as shown in Fig. 5. The high-resolution XPS peaks of Cs, Pb, and Br in Mn-doped samples shift slightly to higher binding energies compared to undoped samples. The Br 3d binding

Table 2 Atomic ratio analysis of samples 0:1–3:1

Mn:Pb	0:1	1:1	2:1	3:1
Mn atomic (%)	0	2.61	7.55	6.62
Pb atomic (%)	100	97.39	92.45	91.38

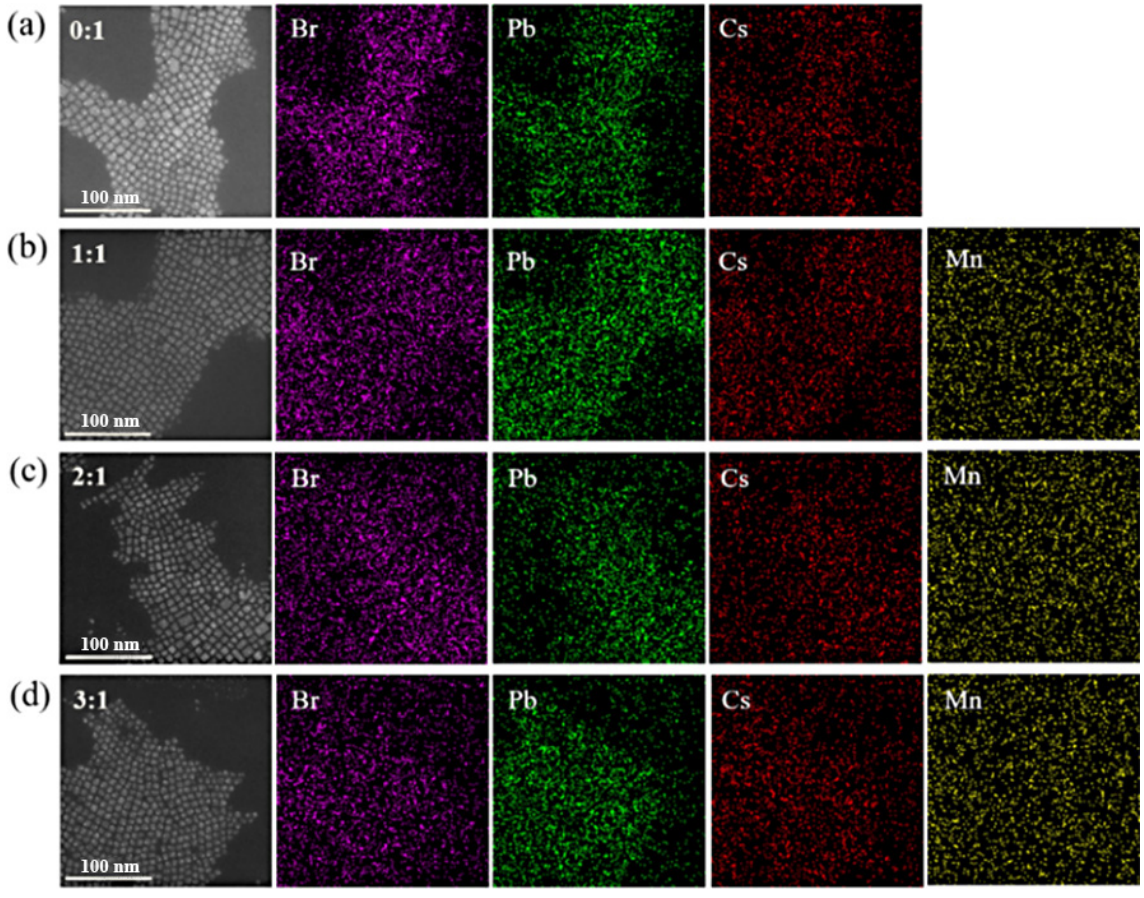

Figure 4 (a)–(d) EDS mapping diagrams of samples 0:1–3:1.

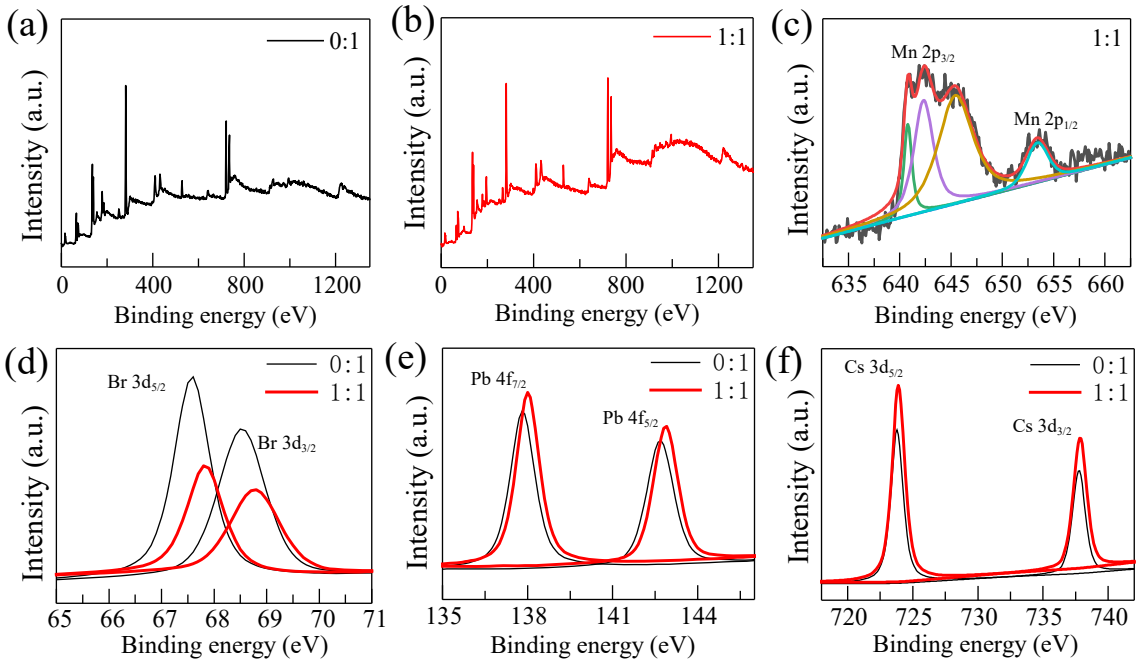

Figure 5 $CsPbBr_3$ quantum dots and Mn:$CsPbBr_3$ quantum dots (Mn:Pb = 1:1): (a)–(b) XPS spectra and (c)–(f) core levels of Mn, Br, Pb, and Cs.

energies of $CsPbBr_3$ quantum dots are 67.6 and 68.5 eV. These correspond to Br $3d_{5/2}$ and Br $3d_{3/2}$, respectively. With the addition of Mn, the binding energies of Br $3d_{5/2}$ and Br $3d_{3/2}$ increase to 67.8 and 68.8 eV, respectively. The binding energy of Pb 4f has two peaks at 137.8 and 142.7 eV, corresponding to Pb $4f_{7/2}$ and Pb $4f_{5/2}$, respectively. After the doping of Mn, the binding energy shifts to the high energy side at 138 and 142.9 eV. Similar to Pb 4f, the binding energy of Cs 3d also shows two peaks. The binding energy of Cs $3d_{5/2}$ increases from 723.8 to 723.9 eV. The binding energy of Cs $3d_{3/2}$ is 737.8 eV, without obvious shift. The slight change in binding energy indicates a small shift in coordination chemistry conditions. When doping with Mn, the octahedral distortion becomes smaller, resulting in a higher binding energy transition. In addition, the valence state of the doped ions was determined by XPS analysis, which confirms the existence of manganese in a divalent form. Also, no other impurities were detected. The synthesis confirmed the sample's purity.

Figure 6(a) is PL spectra of $CsPbBr_3$ QDs and Mn:$CsPbBr_3$ quantum dots dispersed in n-hexane. As shown in Fig. 6(a), after excitation at 385 nm, $CsPbBr_3$ quantum dots emitted a narrow PL signal at 520.7 nm. This is due to radiation attenuation caused by band gap recombination. The proper amount of doping improves the PL of $CsPbBr_3$ quantum dots. A stronger PL intensity means less non-radiative decay, because defects are a key cause for PL quenching. Thus, doping with Mn^{2+} can suppress the structural

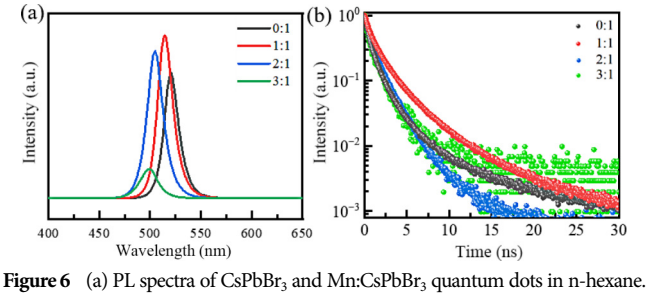

Figure 6 (a) PL spectra of $CsPbBr_3$ and Mn:$CsPbBr_3$ quantum dots in n-hexane. (b) TRPL measurements of $CsPbBr_3$ and Mn:$CsPbBr_3$ quantum dots films.

defects and improve the defect formation energy, which increases the short-range order of the $CsPbBr_3$ structure and ultimately leads to higher luminous efficiency. The PL peaks of the three doped samples were blue-shifted compared to the undoped sample. The peaks were 514.5, 504.8, and 498.3 nm, respectively. Also, it is speculated that, due to the low band gap of $CsPbBr_3$ (2.406 eV, Fig. 7(b)) and the low energy of exciton transition, Mn^{2+} doped $CsPbBr_3$ quantum dots do not exhibit Mn-related PL spectra in the visible spectral region at room temperature.

TRPL is an effective technique to characterize the electron-hole pair recombination dynamics process, and the trap state or impurity level in the perovskite film is evaluated by the carrier lifetime. The room temperature TRPL test was performed on the four quantum dots films, and the results are shown in Fig. 6(b). The TRPL decay curve is fitted by a double exponential decay function to extract the carrier lifetime, as shown in Eq. (1)

$$f(t) = \sum_i A_i \exp(-t/\tau_i) + K \quad (1)$$

The fitting parameters are shown in Table 3. where A_i is the decay amplitude, τ_i is the decay time, and K is a constant. The average PL decay time (τ_{ave}) is quantitatively calculated using the A_i and τ_i values from the above analysis using Eq. (2)

$$\tau_{ave} = \frac{\sum A_i \tau_i^2}{\sum A_i \tau_i} \quad (2)$$

According to Eq. (2), the corresponding average carrier lifetime τ_{ave} is calculated. At room temperature, the carrier lifetime of the $CsPbBr_3$ quantum dot film with a molar ratio of 1:1 is the highest. Compared with the undoped sample, the luminescence decay time is extended from 1.47 to 2.31 ns. The $CsPbBr_3$ quantum dots, after Mn^{2+} doping, have a longer lifetime. This means that the doping passivated the perovskite lattice, reducing defects. So, carriers are less likely to be trapped by defects and suffer non-radiative recombination.

Figure 7 shows the optical absorption properties of $CsPbBr_3$

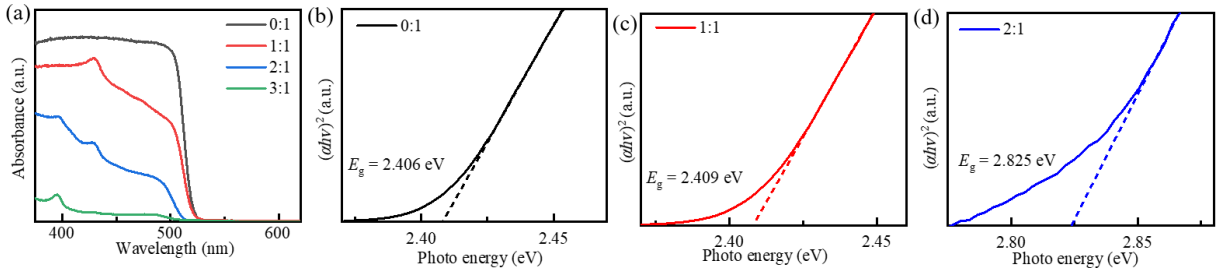

Figure 7 (a) UV–Visible absorption spectra and (b)–(d) the high binding energy cut-off edge of $CsPbBr_3$ and Mn:$CsPbBr_3$ quantum dots in n-hexane.

Table 3 The carrier lifetime parameters extracted by fitting the TRPL curves

Mn:Pb	0:1	1:1	2:1	3:1
A_1	0.69	0.6	0.5	0.62
τ_1 (ns)	0.49	0.71	0.49	0.32
A_2	0.31	0.4	0.47	0.42
τ_2 (ns)	2	2.9	1.7	1.65
τ_{ave} (ns)	1.47	2.31	1.54	1.35

quantum dots dispersed in n-hexane. The absorption spectra of the samples at 0:1 and 1:1 show a sudden absorption starting from about 529 nm. The band gap increases slightly from 2.406 to 2.409 eV. For sample 2:1, it rises to 2.825 eV. This is due to the combined effect of Mn^{2+} doping and a change in particle size [30, 31].

The magnetic properties of Mn:$CsPbBr_3$ quantum dots were confirmed by VSM analysis. Figure 8 shows the field-dependent magnetization measurement (M–H curves) of Mn:$CsPbBr_3$ quantum dots at 300 K. The enlarged M–H curves near H = 0 in Fig. 8(b) have an obvious hysteresis loop. The non-zero values of hysteresis loops and coercivity prove that all samples are ferromagnetic. The ferromagnetism of $CsPbBr_3$ quantum dots may be derived from the spin-splitting states caused by Br vacancies in one-pot preparation [32–33]. VSM measurements show that the saturation magnetization of $CsPbBr_3$ quantum dots at room temperature increases from 1.2657 to 1.9869 emu/g due to the incorporation of Mn^{2+}. This enhances their ferromagnetism.

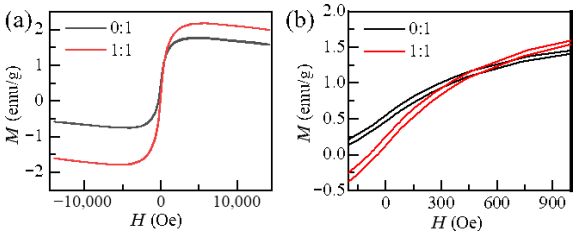

Figure 8 (a) Saturation magnetization curves and (b) local amplification curves of $CsPbBr_3$ and Mn:$CsPbBr_3$ quantum dots at T = 300 K.

Figure 9 shows the effect of a 50 mT static magnetic field on the steady-state PL signal intensity at room temperature. Because the distribution of permanent magnets in space is not uniform, the magnetic field strength is expressed by the magnetic field strength at the sample. The measurement shows that the exposure of the sample to the magnetic field will reduce the PL intensity. Table 4 shows the variation of PL peak values, the PL of the four samples decreased by 1.33%, 5.91%, 1.96%, and 1.71%, respectively. Figure 9(c) shows the PL changes of two cycles of adding and removing a magnetic field. In the sample 1:1, due to the successful incorporation of Mn^{2+}, more spin-polarized electrons are introduced, and the charge recombination is reduced under the action of magnetic field, so the PL intensity decreases due to the magnetic field. The PL spectra of samples 2:1 and 3:1 are not significantly affected by the magnetic field, which may be due to the formation of impurity phases. Combined with Figs. 9(c) and 9(d), it can be seen that this process is reversible. Removing the static magnetic field, the PL signal intensity can be completely restored. The doping of Mn makes the $CsPbBr_3$ quantum dots more responsive to magnetic field, allowing for their application in spintronic devices.

Table 4 The fluorescence intensity changes at 50 mT magnetic field intensity

Mn:Pb	0:1	1:1	2:1	3:1
PL	30,443.46	39,611	35,819	7198
PL under magnetic field	30,032.47	37,269	35,116	7075
Decrease ratio (%)	1.350	5.912	1.963	1.739

4 Conclusions

In this work, $CsPbBr_3$ quantum dots with different Mn^{2+} concentrations were synthesized by one-pot method in air. The quantum dots were uniform and not agglomeration. The experimental results show that the smaller Mn^{2+} partially replaces Pb^{2+}. This causes the lattice contraction of $CsPbBr_3$ perovskite. It improves the exciton binding energy of $CsPbBr_3$ quantum dots and reduces the defects of $CsPbX_3$ quantum dots. Thus, it stabilizes the

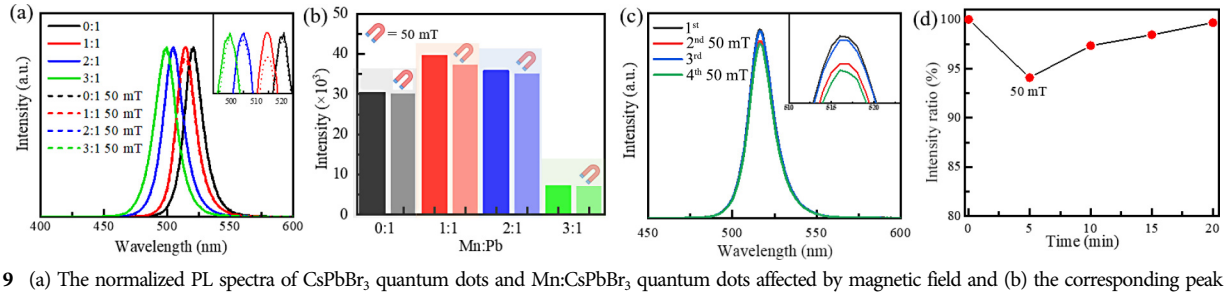

Figure 9 (a) The normalized PL spectra of $CsPbBr_3$ quantum dots and Mn:$CsPbBr_3$ quantum dots affected by magnetic field and (b) the corresponding peak change histogram. (c) The PL change diagram of two cycles with and without magnetic field, and (d) the PL recovery diagram of withdrawing magnetic field of sample 1:1.

lead halide perovskite and improves the crystallinity and PL properties of $CsPbBr_3$ quantum dots. The appropriate amount of Mn doping does not affect the structure of $CsPbBr_3$ quantum dots. VSM measurements show that the saturation magnetization at room temperature increases from 1.2657 to 1.9869 emu/g with the doping of Mn^{2+}. Even a low Mn^{2+} doping level (3.46%) can significantly enhance the ferromagnetism of $CsPbBr_3$. In theory, the enhancement of magnetism has a positive effect on spin polarization. The testing of the PL spectrum of Mn:$CsPbBr_3$ quantum dots under a 50 mT static magnetic field proved that proper Mn doping makes $CsPbBr_3$ quantum dots more sensitive to the magnetic field.

Doping $CsPbBr_3$ quantum dots with the proper amount of Mn^{2+} affects their structure and optical properties. It also enhances their ferromagnetism. This offers a new option for developing all-inorganic perovskite quantum dots for room-temperature spintronic device.

Data availability

All data needed to support the conclusions in the paper are presented in the manuscript. Additional data related to this paper may be requested from the corresponding author upon request.

Acknowledgements

This work was supported by the Hubei province Natural Science Fund for Distinguished Young Scholars (No. 201CFA077); and Hubei province "Chu Tian Talent" scientific and technological innovation team.

Declaration of competing interest

All the contributing authors report no conflict of interests in this work.

Author contribution statement

M. W. C.: Project administration, data curation, writing manuscript, experimental design. C. G. S.: Data curation, writing manuscript. W. H.: Validation. Y. P. Y.: Project administration. J. S.: Funding acquisition, project administration.

Use of AI statement

None.

References

[1] Cornia, A.; Seneor, P. The molecular way. *Nat. Mater.* **2017**, *16*, 505–506.
[2] Sierra, J. F.; Fabian, J.; Kawakami, R. K.; Roche, S.; Valenzuela, S. O. Van der Waals heterostructures for spintronics and opto-spintronics. *Nat. Nanotechnol.* **2021**, *16*, 856–868.
[3] Shao, D. F.; Zhang, S. H.; Li, M.; Eom, C. B.; Tsymbal, E. Y. Spin-neutral currents for spintronics. *Nat. Commun.* **2021**, *12*, 7061.
[4] Kim, S. K.; Beach, G. S. D.; Lee, K. J.; Ono, T.; Rasing, T.; Yang, H. Ferrimagnetic spintronics. *Nat. Mater.* **2022**, *21*, 24–34.
[5] Gish, J. T.; Lebedev, D.; Song, T. W.; Sangwan, V. K.; Hersam, M. C. Van der Waals opto-spintronics. *Nat. Electron.* **2024**, *7*, 336–347.
[6] Shumilin, A. V.; Shamirzaev, T. S.; Smirnov, D. S. Spin light emitting diode Based on exciton fine structure tuning in quantum dots. *Phys. Rev. Lett.* **2024**, *132*, 076202.
[7] Kim, Y. H.; Zhai, Y. X.; Lu, H. P.; Pa, X.; Xiao, C. X.; Gaulding, E. A.; Harvey, S. P.; Berry, J. J.; Vardeny, Z. V.; Luther, J. M. et al. Chiral-induced spin selectivity enables a room-temperature spin light-emitting diode. *Science* **2021**, *371*, 1129–1133.
[8] Liu, J.; Peng, Z. S.; Cai, J. Z.; Yue, J. Y.; Wei, H. N.; Impundu, J.; Liu, H.; Jin, J. Y.; Yang, Z.; Chu, W. G. et al. A room-temperature four-terminal spin field effect transistor. *Nano Today* **2021**, *38*, 101138.
[9] Eberle, F.; Schuh, D.; Grünewald, B.; Bougeard, D.; Weiss, D.; Ciorga, M. Controlled rotation of electrically injected spins in a nonballistic spin-field-effect transistor. *Nano Lett.* **2023**, *23*, 4815–4821.
[10] Kang, K. F.; Qiu, Y. C.; Watanabe, K.; Taniguchi, T.; Shan, J.; Mak, K. F. Double quantum spin Hall phase in Moiré WSe_2. *Nano Lett.* **2024**, *24*, 14901–14907.
[11] Jang, H. J.; Richter, C. A. Organic spin-valves and beyond: Spin injection and transport in organic semiconductors and the effect of interfacial engineering. *Adv. Mater.* **2017**, *229*, 1602739.
[12] Yang, X. L.; Guo, A. K.; Guo, L. D.; Liu, Y. Q.; Sun, X. N.; Guo, Y. L. Organic semiconductors for room-temperature spin valves. *ACS Mater. Lett.* **2022**, *4*, 805–814.
[13] Tian, Y. L.; Cao, H. Q.; Yang, H. J.; Yao, W. Q.; Wang, J. O.; Qia, Z. R.; Cheetham, A. K. Electron spin catalysis with graphene belts. *Angew. Chem., Int. Ed.* **2023**, *62*, e202215295.
[14] Sun, B.; Yan, Z.; Cao, Y.; Ding, S. S.; Li, R. J.; Ma, B.; Li, X. Y.; Yang, H.; Yin, W.; Zhang, Y. M. et al. Intrinsic ferromagnetic semiconductors with high saturation magnetization from hybrid perovskites. *Adv. Mater.* **2023**, *35*, 2303945.
[15] Giovanni, D.; Ma, H.; Chua, J.; Grätzel, M.; Ramesh, R.; Mhaisalkar, S.; Mathews, N.; Sum, T. C. Highly spin-polarized carrier dynamics and ultralarge photoinduced magnetization in $CH_3NH_3PbI_3$ Perovskite Thin Films. *Nano Lett.* **2015**, *15*, 1553–1558.
[16] Zhang, H. C.; Zhai, Z. H.; Bi, Z. X.; Gao, H.; Ye, M.; Xu, Y.; Tan, H. R.; Yang, L. Y. Spin coherence and spin relaxation in hybrid organic-inorganic lead and mixed lead-tin perovskites. *Nano Lett.* **2023**, *23*, 7914–7920.
[17] Burschka, J.; Pellet, N.; Moon, S. J.; Humphry-Baker, R.; Gao, P.; Nazeeruddin, M. K.; Grätzel, M. Sequential deposition as a route to high-performance perovskite-sensitized solar cells. *Nature* **2013**, *499*, 316–319.
[18] Li, Y. X.; Zhang, X. Y.; Huang, H.; Kershaw, S. V.; Rogach, A. L. Advances in metal halide perovskite nanocrystals: Synthetic strategies, growth mechanisms, and optoelectronic applications. *Mater. Today* **2020**, *32*, 204–221.
[19] Kovalenko, M. V.; Protesescu, L.; Bodnarchuk, M. I. Properties and potential optoelectronic applications of lead halide perovskite nanocrystals. *Science* **2017**, *358*, 745–750.
[20] Huang, H.; Polavarapu, L.; Sichert, J. A.; Susha, A. S.; Urban, A. S.; Rogach, A. L. Colloidal lead halide perovskite nanocrystals: Synthesis, optical properties and applications. *NPG Asia Mater.* **2016**, *8*, e328.
[21] Lee, M. M.; Teuscher, J.; Miyasaka, T.; Murakami, T. N.; Snaith, H. J. Efficient hybrid solar cells based on meso-superstructured organometal halide perovskites. *Science* **2012**, *338*, 643–647.
[22] Kim, Y. C.; Kim, K. H.; Son, D. Y.; Jeong, D. N.; Seo, J. Y.; Choi, Y. S.; Han, I. T.; Lee, S. Y. Park, N. G. Printable organometallic perovskite enables large-area, low-dose X-ray imaging. *Nature* **2017**, *550*, 87–91.
[23] Náfrádi, B.; Szirmai, P.; Spina, M.; Lee, H.; Yazyev, O. V.; Arakcheeva, A.; Chernyshov, D.; Gibert, M.; Forró, L.; Horváth, E. Optically switched magnetism in photovoltaic perovskite CH_3NH_3(Mn:Pb)I_3. *Nat. Commun.* **2016**, *7*, 13406.
[24] Rajamanickam, N.; Chowdhury, T. H.; Isogami, S.; Islam, A. Magnetic properties in $CH_3NH_3PbI_3$ perovskite thin films by Mn doping. *J. Phys. Chem. C* **2021**, *125*, 20104–20112.
[25] Kanoun, M. B.; Goumri-Said, S. Insights into the impact of Mn-doped

inorganic $CsPbBr_3$ perovskite on electronic structures and magnetism for photovoltaic application. *Mater. Today Energy* **2021**, *21*, 100796.

[26] Parobek, D.; Roman, B. J.; Dong, Y. T.; Jin, H.; Lee, E.; Sheldon, M.; Son, D. H. Exciton-to-dopant energy transfer in Mn-doped cesium lead halide perovskite nanocrystals. *Nano Lett.* **2016**, *16*, 7376–7380.

[27] Liu, W. Y.; Lin, Q. L.; Li, H. B.; Wu, K. F.; Robel, I.; Pietryga, J. M.; Klimov, V. I. Mn^{2+}-doped lead halide perovskite nanocrystals with dual-color emission controlled by halide content. *J. Am. Chem. Soc.* **2016**, *138*, 14954–14961.

[28] Yeh, I. H.; Ghobadifard, M.; Feng, L.; Galievsky, V.; Radovanovic, P. V. Origin of dopant-carrier exchange coupling and excitonic zeeman splitting in Mn^{2+}-doped lead halide perovskite nanocrystals. *Nano Lett.* **2024**, *24*, 10554–10561.

[29] Jung, H. S.; Choe, H.; Park, J.; Kim, Y.; Oh, S. J.; Ryu, S. J.; Na, H. K.; Lee, S. J.; Neuman, K. C.; Cho, J. et al. Dual-emissive Mn-doped lead halide perovskite nanocrystals as background-suppressed latent fingerprint detection probes. *ACS Appl. Mater. Interfaces* **2023**, *15*, 51593–51605.

[30] Protesescu, L.; Yakunin, S.; Bodnarchuk, M. I.; Krieg, F.; Caputo, R.; Hendon, C. H.; Yang, R. X.; Walsh, A.; Maksym, V.; Kovalenko, M. V. Nanocrystals of cesium lead halide perovskites ($CsPbX_3$, X=Cl, Br, and I): Novel optoelectronic materials showing bright emission with wide color gamut. *Nano Lett.* **2015**, *15*, 3692–3696.

[31] Wang, C. W.; Liu, X. H.; Qiao, T.; Khurana, M.; Akimov, A. V.; Son, D. H. Photoemission of the upconverted hot electrons in Mn-doped $CsPbBr_3$ nanocrystals. *Nano Lett.* **2022**, *22*, 6753–6759.

[32] Sun, Z. G.; Cai, B.; Chen, X.; Wei, W. X.; Li, X. M.; Yang, D. D.; Meng, C. F.; Wu, Y.; Zeng, H. B. Prediction and observation of defect-induced room-temperature ferromagnetism in halide perovskites. *J. Semicond.* **2020**, *41*, 122501.

[33] Kumar, V.; Chauhan, H. C.; Nagal, V.; Hafiz, A. K.; Singh, K. Lattice-distortion-induced change in the magnetic properties in Br-defect host $CsPbBr_3$ perovskite quantum dots. *J. Phys. Chem. Lett.* **2023**, *14*, 888–896.